

See discussions, stats, and author profiles for this publication at: <https://www.researchgate.net/publication/278687973>

Influence of cryorolling on microstructure and mechanical properties of a cast hypoeutectic Al–Si alloy

Article in Materials Science and Engineering A · July 2015

DOI: 10.1016/j.msea.2015.06.019

CITATIONS

59

READS

1,029

2 authors:



Jose Immanuel Rajan
Indian Institute of Technology Bhilai

51 PUBLICATIONS 557 CITATIONS

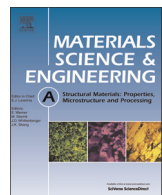
[SEE PROFILE](#)



Sushanta Panigrahi
Indian Institute of Technology Madras

103 PUBLICATIONS 4,787 CITATIONS

[SEE PROFILE](#)



Influence of cryorolling on microstructure and mechanical properties of a cast hypoeutectic Al–Si alloy



R.J. Immanuel, S.K. Panigrahi*

Department of Mechanical Engineering, Indian Institute of Technology Madras, Chennai 600036, India

ARTICLE INFO

Article history:

Received 16 May 2015

Received in revised form

3 June 2015

Accepted 4 June 2015

Available online 9 June 2015

Keywords:

Al–Si cast alloy

A356

Cryorolling

Microstructural modification

Mechanical properties

ABSTRACT

Cast Al–Si alloys often show poor tensile strength, less ductility and poor fatigue performance due to cast microstructure and presence of porosity. An attempt has been made to improve mechanical properties of a cast hypoeutectic Al–Si alloy (A356) by cryorolling. As cast Al–Si alloy (A356) processed by cryorolling at different imposed strain levels was subjected to microstructural analysis and mechanical testing. Cryorolling resulted in break up and uniform distribution of coarse acicular eutectic particles in the aluminium matrix, elimination of casting porosity, microstructural refinement and significant accumulation of dislocation density. These microstructural changes resulted in significant improvement in the strength (248%) and ductility (37%). The influence of cryorolling on mechanism of microstructural modification, strengthening mechanism and failure mechanism are studied in detail.

© 2015 Elsevier B.V. All rights reserved.

1. Introduction

Al–Si cast alloys are extensively used in automobile, aerospace and various other general engineering applications due to their high strength to weight ratio, excellent castability, low thermal coefficient, high corrosion resistance and good wear resistance [1–5]. However, these alloys often possess low strength, insufficient ductility and poor machinability due to the presence of large, irregularly shaped and unevenly distributed hard and brittle silicon containing eutectic particles [6]. Many attempts have been made to enhance the mechanical properties of these Al–Si cast alloy systems by microstructural modification. Several researchers were successful in modifying the morphology of the silicon eutectic particles (silicon particles, hereafter) and the size of the dendrite structure by adding trace amount of different alloying elements [7,8]. Effect of heat treatment on the microstructural modification has been studied by Zhu et al. [9] on an age hardenable A356 alloy. They found that the T6 heat treatment improves the mechanical properties by spheroidization of the silicon particles and formation of fine Mg₂Si precipitates. However, the improvement in the mechanical properties by thermal treatment is not much significant because of the non-uniform distribution of silicon particles in the matrix, which makes the material to fail through inter-dendritic crack propagation.

Severe plastic deformation (SPD) methods are found to be attractive tools in refining the microstructure of the materials [10,11]. A lot of work has been done on the SPD processing of wrought aluminium alloys [12]. However, the work on SPD of cast aluminium alloys is few in the literature. Gutierrez et al. [13] were successful in processing an Al–Si hypoeutectic alloy using equal channel angular pressing (ECAP). They obtained fine grains with uniform distribution of silicon particles. Cepeda et al. [14] studied the microstructural evolution of a hypo eutectic Al–Si alloy processed by high pressure torsion (HPT) and they observed fine particle distribution with nano-grained matrix. Friction stir processing was also found to be an effective tool in refining the particles and redistributing them thoroughly in the aluminium matrix [3,6,15].

Though the aforementioned SPD processes were successful in refining the microstructure and enhancing the mechanical properties, they possess certain demerits. The processing temperature of these SPD techniques is high. Even though some of the SPD processes were performed at room temperature [3–5], the material experiences high temperature during the process. Ghazani et al. [16] demonstrated that the temperature of an Al–Mg alloy reaches about 100 °C when the sample is ECAPed at room temperature due to intense plastic deformation and large amount of frictional heat generated during the SPD process. At these deformation temperatures, aluminium recovers by annihilating the stored dislocations because of its high stacking fault energy [17] and hence, large strain is needed to refine the microstructure. Also, in age hardenable alloy systems, the high process temperature

* Corresponding author.

E-mail address: skpanigrahi@iitm.ac.in (S.K. Panigrahi).

gives rise to dynamic precipitation. The precipitates that evolve during the SPD process are coarse in nature and hence do not contribute much to the enhancement in mechanical properties. Also, the dynamic precipitation depletes the solute concentration in the solid solution [18], which restricts the use of post-process aging to produce nano-precipitates. Post-process solution treatment can be used to dissolve the dynamically emerged precipitates back into the matrix and then the sample can be peak aged to obtain a higher strength. However, the high temperature during the solution treatment activates annihilation of dislocation and also partially coarsens the fine grain which greatly affects the strength of the material. Therefore, a low temperature SPD process is desirable for the processing of age hardenable Al-Si cast alloys to improve the mechanical properties.

Cryorolling is identified as a potential low temperature SPD route for effective microstructural refinement [19–22]. In 2000, Wang et al. [19] cryorolled a pure copper upto a strain of 2.3 and obtained ultrafine grained microstructure with high strength and ductility. From then onwards, a lot of studies have been reported in cryorolling of different alloys. Though a large number of research works have been carried out on cryorolling of various alloy systems, the literature available on cast alloy systems is very limited. Markushev et al. [23] have performed cryorolling on a D16 (Al-4.4% Cu) cast alloy. However, a pre-process ECAP has been done to remove the cast dendritic microstructure. Few literature [24,25] is also available on cryorolling of aluminium in-situ composites which are fabricated by stir casting route. With this background, the current research aims in studying the effect of cryorolling on a cast aluminium alloy, A356.

In the present work, cryorolling was implemented on a cast hypo-eutectic Al-Si alloy, A356. The prime objectives of the present work are (a) to explore the feasibility of cryorolling on Al-Si cast alloys; (b) to investigate the extent of microstructural modification through cryorolling and (c) to correlate the microstructural evolution during cryorolling with the obtained mechanical properties and establish the deformation and failure mechanism.

2. Materials and methods

A commercial grade of A356 has been procured from Sargam Metals Pvt. Ltd., India which is from Al-Si alloy series. The compositional analysis is done using optical emissive spectroscopy (OES) as per ASTM E1251 standards and is given in Table 1.

Plates with initial thickness of 8 mm were cut from the cast ingots and then solution treated at 540 °C for 8 h followed by cold-water quenching. Cryorolling was done with a rolling mill of diameter 110 mm at the speed of 8 rpm. The final reduction to 1 mm was obtained in multiple passes. Between each pass, the samples were dipped in liquid nitrogen for 15 min to ensure a mere constant temperature throughout the process. To study the microstructural evolution in the cryorolling process, two different thickness reductions were considered which is given in Table 2. From now onwards, the As cast, solution treated, 50% cryorolled and 87.5% cryorolled samples will be referred as AC, ST, 50CR and 87CR respectively.

To study, compare and understand the microstructural evolution during solution treatment and cryorolling, microstructural

Table 1
Chemical composition.

Si	Mg	Mn	Fe	Cu	Ti	Zn	Others	Al
6.62	0.357	0.092	0.324	0.0783	0.0329	0.0233	0.03	Bal.

Table 2
Sample conditions and nomenclature.

Material	Thickness (mm)	Thickness reduction (%)	Equivalent strain, ϵ
AC	8	–	–
ST	8	–	–
50CR	4	50	0.69
87CR	1	87.5	2.08

analyses were conducted using optical microscopy, scanning electron microscopy (SEM) and transmission electron microscopy (TEM). For optical microscopy, standard metallographic procedure is followed as per ASTM E3 standards for sample preparation. Samples were mounted on a cold setting epoxy mould and then ground using series of emery from 180 to 2000 grit size followed by 3 micron and 1 micron diamond polishing. Final polishing was done using 0.2 micron colloidal silica. Optical microscopic images were captured in a Quasmo MR 5000 inverted metallurgical microscope in bright field mode. SEM studies were carried out in a FEI Quanta 200 machine operating at 30 kV.

Quantitative analysis of the silicon particles was carried out using ImageJ [26]. Particle size, D , was calculated using the relation, $D = P/\pi$, where P is the perimeter of the silicon particle obtained from ImageJ. About 700 particles per material condition were considered to plot the histograms. A threshold of 1 μm was set as the minimum particle size to avoid capturing background noise. This limits our study and any particle that are smaller than 1 μm are not considered. For calculating the aspect ratio, the particles are assumed to be a perfect ellipse and the aspect ratio is calculated as the ratio between the major and minor axes.

A FEI Tecnai equipment operating at an accelerating voltage of 200 kV was used for TEM studies. Samples for TEM study were mechanically thinned down to 80 micron thickness and then electro-chemically polished with an electrolyte containing 20% nitric acid and 80% methanol at -20 °C using a twin-jet electro-polishing machine, TenuPol-5.

X-ray diffraction (XRD) analysis was carried out using a Bruker AXS D8 Discover diffractometer with Copper source, K_α radiation ($\lambda = 1.54 \text{ \AA}$). Samples were prepared as per the standard metallographic procedure mentioned above to remove any oxide layer present and then electro-polished with the aforementioned electrolyte to remove any strain imposed during the preparation process.

The influence of cryorolling on mechanical behaviour was studied by conducting hardness and tensile testing on the as cast (AC), solution treated (ST) and cryorolled samples (50CR and 87CR). Micro-indentation hardness test was carried out in a Future Tech FM-707 with the test load of 0.2 kg and a dwell time of 15 s as per ASTM E384 standards. Samples for hardness test were mounted in an epoxy mould and then polished up to 1 micron diamond polish. An average of at least 10 data points in each material condition were taken to get the hardness value.

Tensile test was conducted in an INSTRON 3365 machine at an initial strain rate of $2.5 \times 10^{-3} \text{ s}^{-1}$. Tensile samples are made as per ASTM E8 standards with the gauge dimensions of 25 mm length and 6 mm width.

3. Results

3.1. Microstructural evolution

Microstructure of AC, ST and CR samples are shown in Fig. 1 in a three dimensional perspective view. The as cast material (Fig. 1(a)) consists of dendrites of α -aluminium matrix, with inter-dendrite

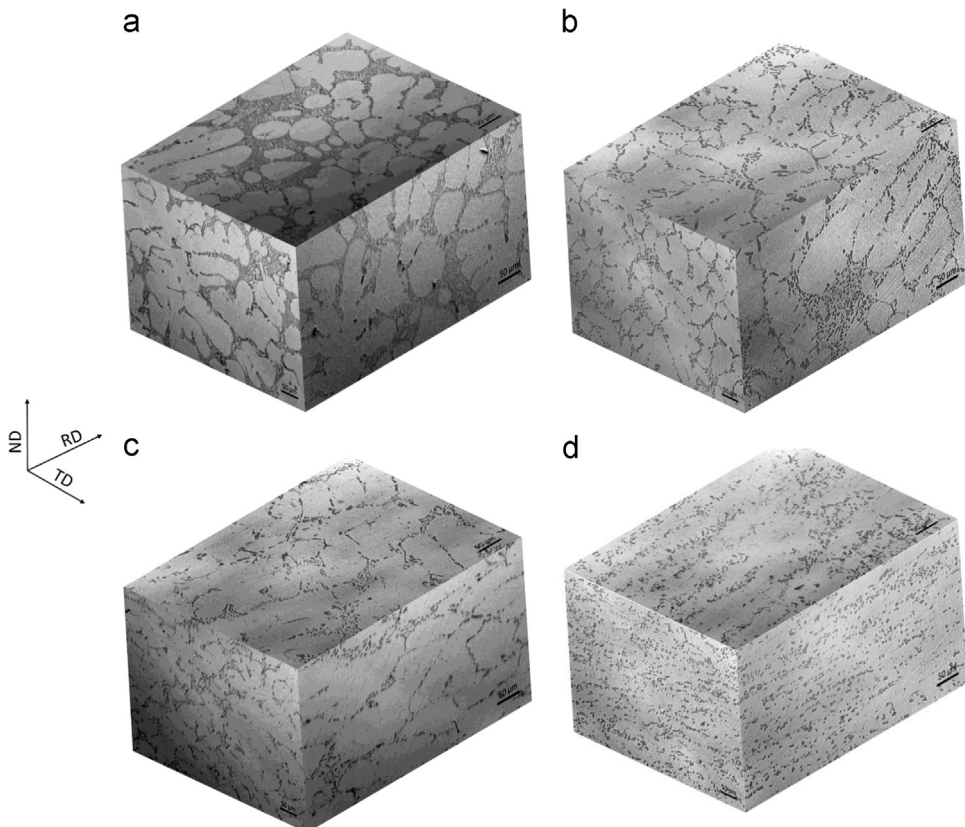


Fig. 1. Three dimensional microstructure of (a) AC, (b) ST, (c) 50CR and (d) 87CR materials. (images magnification: 200×. The scale bar in the images indicates 50 μm).

Al-Si eutectic regions containing coarse acicular shaped silicon particles. These silicon particles got spheroidized after solution treatment (Fig. 1(b)). The evolution of microstructure in 50% rolled (50CR) and 87.5% rolled (87CR) material is shown in Fig. 1(c) and 1

(d) respectively. No significant particle distribution is observed in 50CR. However, the rolling strain has an impact on the dendrite structure with elongation of dendrites along the rolling direction. In 87CR, the silicon particles became finer and more uniformly

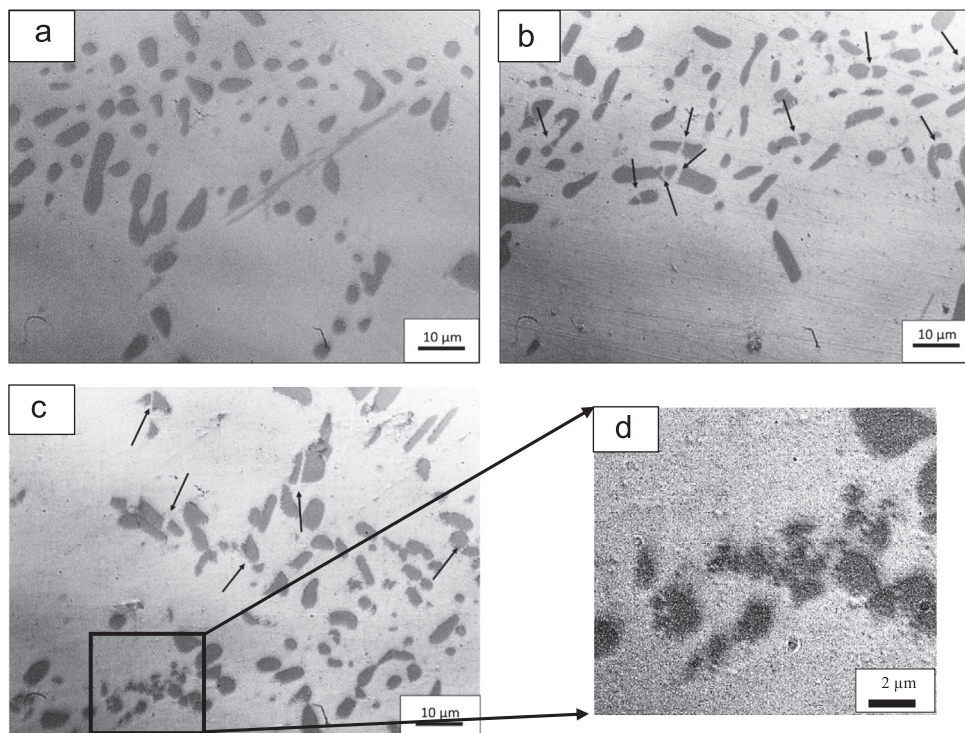


Fig. 2. High magnification OM images of (a) ST, (b) 50CR and (c) 87CR showing the particle morphology before and after rolling. Arrows in the images show fracture of the silicon particles. Zones marked in (c) shows secondary fracture of particles which is magnified in (d).

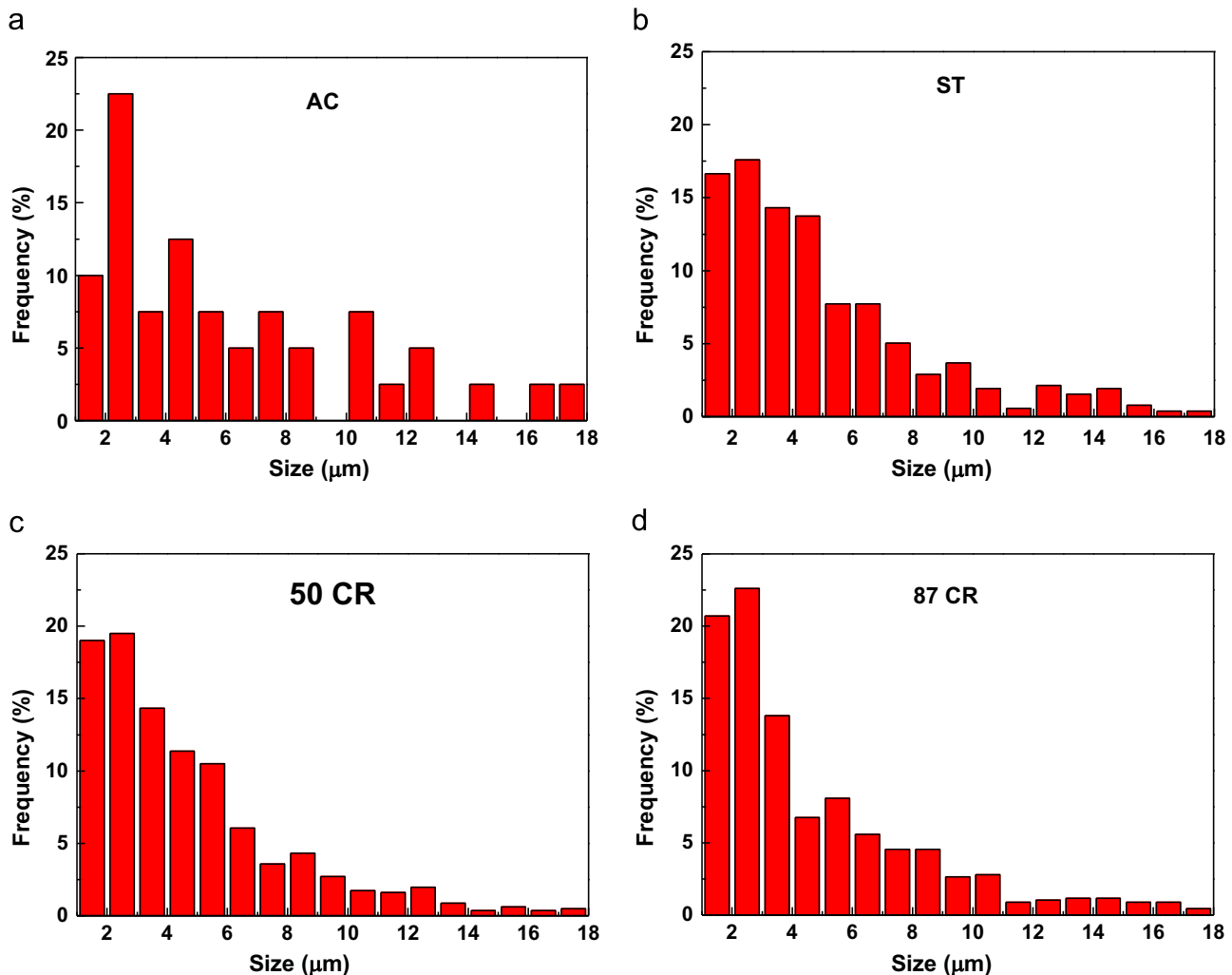


Fig. 3. Histograms of the particle size in (a) AC, (b) ST, (c) 50CR and (d) 87CR.

distributed in the aluminium matrix.

In order to study the particle evolution, high magnification microstructures of ST, 50CR and 87CR samples at the ND plane (top face in Fig. 1) were obtained and shown in Fig. 2. During the initial stage of cryorolling (50CR), the silicon particle with large aspect ratio fractures first which is indicated by arrows in Fig. 2(b). After rolling to 87.5% strain, the fractured particles get refined further by secondary fracture (Fig. 2(c) and (d)).

The histograms of size and aspect ratio of silicon particles are given in Fig. 3 and Fig. 4 respectively. The size and aspect ratio of silicon particles in the cast material is spread over the range of 1–18 μm (Fig. 3(a)) and 1–8 (Fig. 4(a)) respectively. After solution treatment, the size distribution trend converges towards the lower particle size (Fig. 3(b)). Also, the shape of the particles approaches sphere with less aspect ratio (Fig. 4(b)) and hence the process of solution treatment is also called as spheroidization heat treatment.

The shape and aspect ratio of the silicon particles after cryorolling reduces with increase in the rolling strain. In 87CR material, 44% of the silicon particles are less than 3 microns and about 50% of the silicon particles lie in the range of 1–4 μm (Fig. 3(d)). The aspect ratio of most of the particles ($> 80\%$) are less than 2 in 87CR material (Fig. 4(d)). This is almost equal to that of the ST material where 82% of the particles are having aspect ratio less than 2. However, the intermediate 50CR material shows a different trend in which the particle size decreases (Fig. 3(c)) with the aspect ratio increasing than that of the ST material (Fig. 4(c)).

The porosity in the solution treated material is found to be 2.67% and the micro-pores are completely eliminated after cryorolling. High magnification image analysis is done at 1000 \times on the processed material at multiple locations (images not shown) and the elimination of porosity is confirmed.

TEM analysis was carried out in order to study the microstructural evolution during cryorolling and is shown in Fig. 5. The TEM image of the aluminium matrix in the 50CR sample (Fig. 5(a)) shows the presence of sub-cell structures indicated by arrows. In 87CR, the cell structure got refined further which is shown in Fig. 5(c). The matrix–particle interface zone of 50CR and 87CR materials is shown in Fig. 5(b) and Fig. 5(d) respectively. In both the 50CR and 87CR materials, the size of the cell structure at the interface (Fig. 5(b) and (d)) is found to be smaller than that observed at the central matrix zone (Fig. 5(a) and (c)).

The XRD patterns of ST, 50CR and 87CR samples are shown in Fig. 6. It is observed that the peak height pattern changes from ST to 87CR (Fig. 6(a)) which is because of the texture induced due to the rolling strain. But any quantitative study regarding the texture is beyond the scope of this research work.

Fig. 6(b) shows the magnified view of the [111] peak of aluminium in both ST and 87CR samples. After cryorolling, the [111] peak has shifted towards the lower 2θ angles. Accumulation of dislocation is quantified based on the broadening of XRD peaks.

Dislocation densities (ρ) of ST, 50CR and 87CR materials are calculated using the following relation [25]:

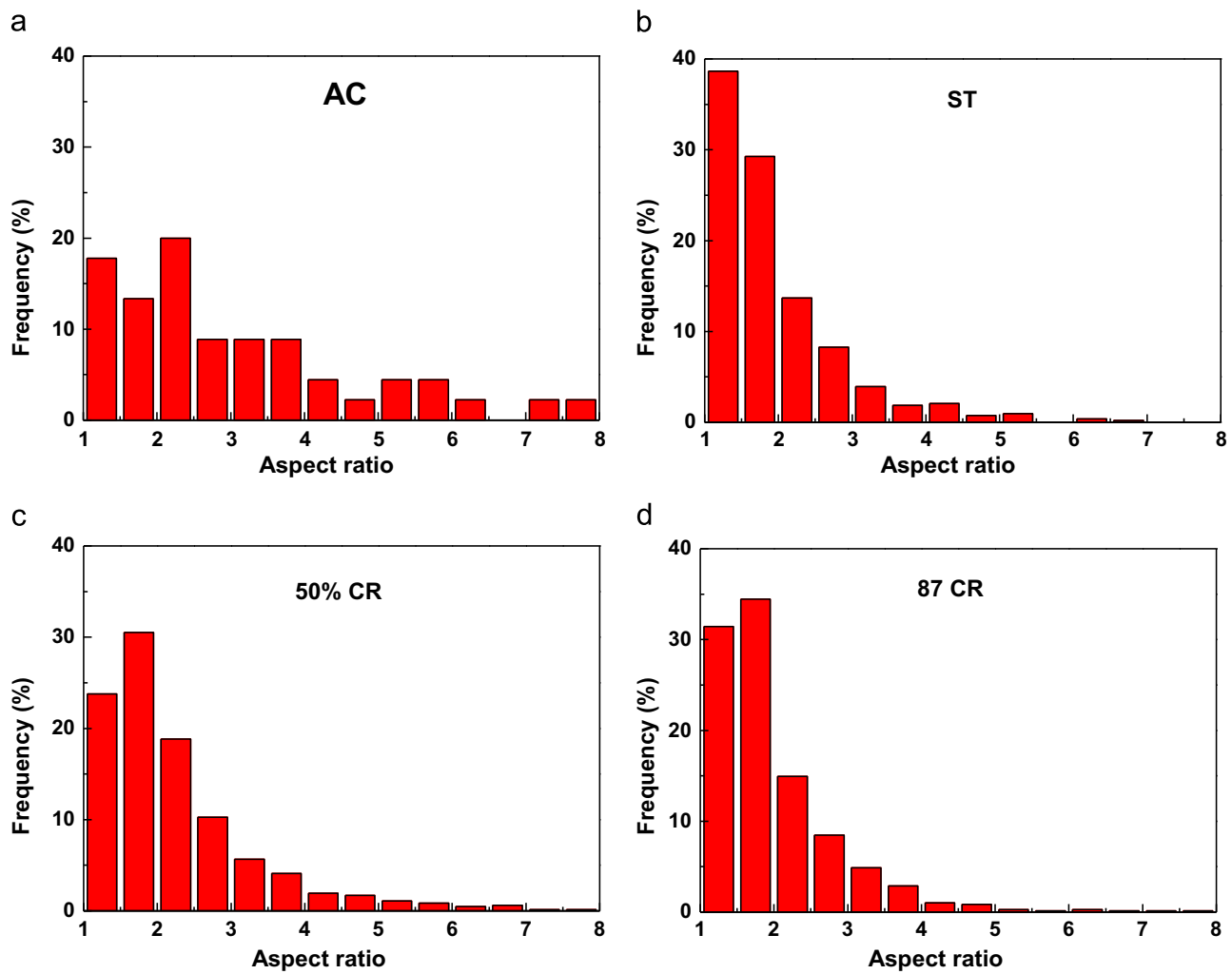


Fig. 4. Histograms of the particle aspect ratio in (a) AC, (b) ST, (c) 50CR and (d) 87CR.

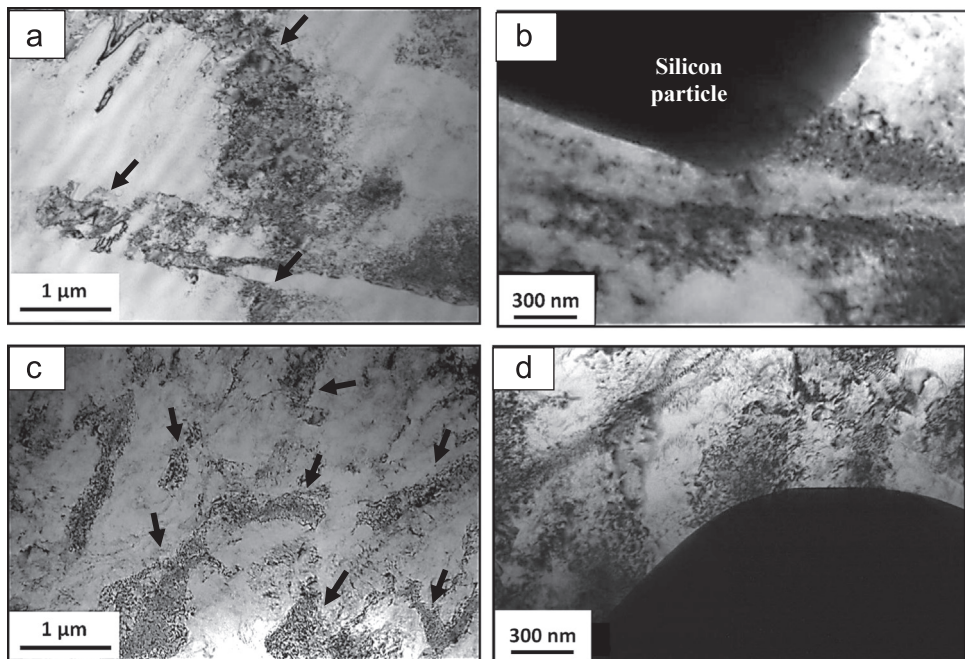


Fig. 5. TEM images of (a) & (b) 50CR and (c) & (d) 87CR material. (a) & (c) Low magnification images showing cell structure (shown with black arrows) formation in the aluminium matrix. (b) & (d) High magnification images at the interface between the aluminium matrix and silicon particle showing the accumulation of dislocations at the interface.

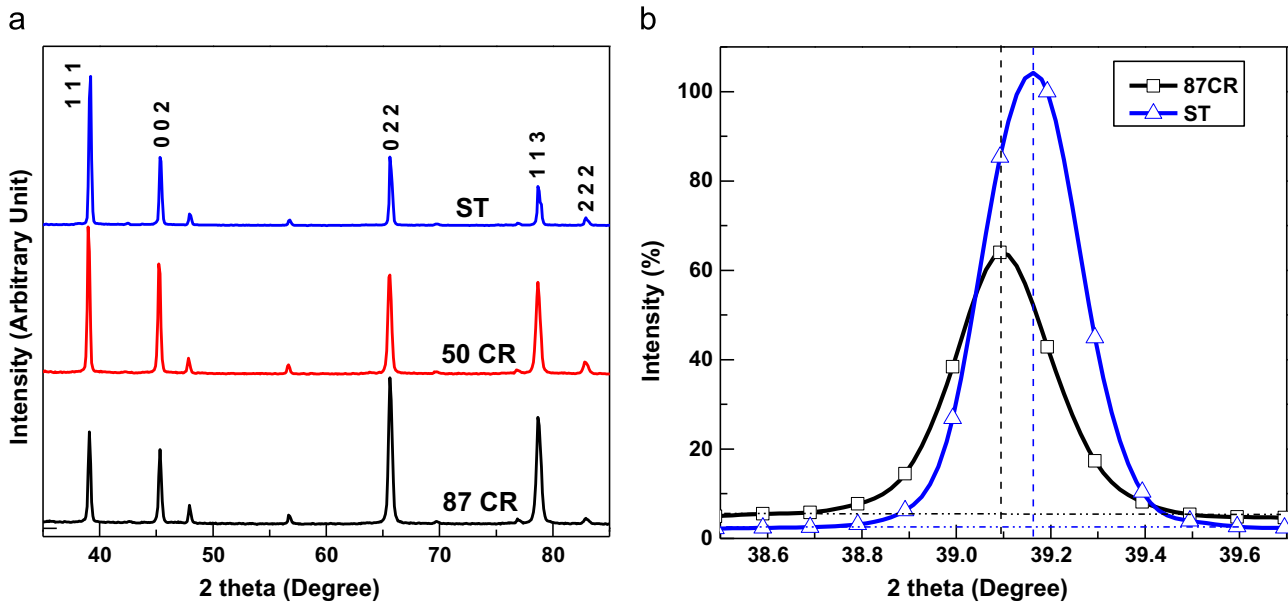


Fig. 6. (a) XRD indexed pattern of ST, 50CR and 87CR materials and (b) the magnified view of the [111] peak of aluminium in both the ST and 87CR materials. The vertical and horizontal lines in (b) show the peak centres and background intensities respectively.

$$\rho = \frac{2\sqrt{3}\varepsilon}{Db} \quad (1)$$

where b is the Burgers vector; D is the domain size and ε is the root mean square (RMS) of the micro-strain obtained at different crystallographic directions. Both the domain size, D and the micro-strain, ε are obtained by the Williamson–Hall method [27,28] using X'pert HighScore Plus. This approach considers the broadening of peak coming from both crystallite size and the strain which is given by the equation

$$B \cos \theta_b = \frac{\lambda K}{D} + \varepsilon \sin \theta_b \quad (2)$$

where B is the peak width measured in terms of full width-half maximum (FWHM), θ_b is the Bragg angle, K is a constant taken as 0.9 [29], and λ is the wavelength of the incident radiation. In order to get the strain and the domain size, the peak width has to be compensated for instrumental broadening. For this, XRD pattern of a fully annealed sample is obtained and the Gauss and Lorentz coefficients corresponding to the XRD peaks of annealed sample is set as the default parameters for the line profile analysis. The calculated dislocation density is given in Table 3.

3.2. Mechanical properties

The Vickers micro-indentation hardness results of the cast, solution treated and cryorolled samples are shown in Fig. 7. In each material condition, hardness values were recorded both at the eutectic zone and in the matrix region. In the AC sample, both the matrix and the eutectic zone showed a very less hardness value of about 60 HV. Both the matrix and the eutectic zone hardness increased after solution treatment with 82 HV and

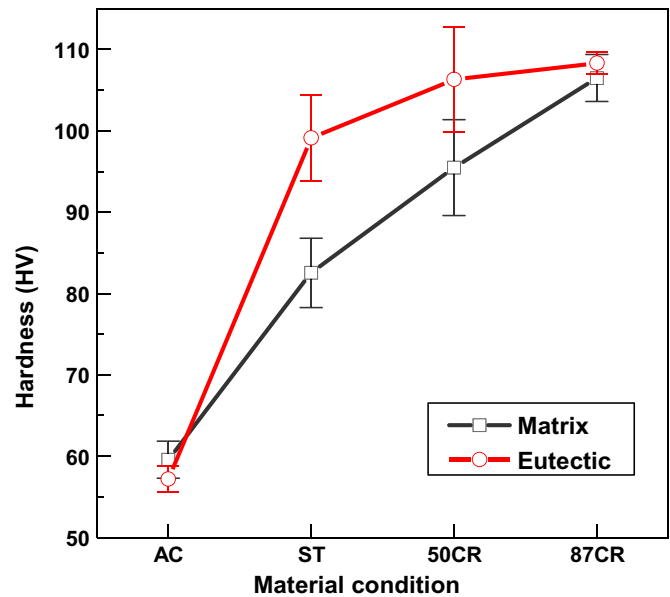


Fig. 7. Micro-indentation hardness of AC, ST and 87CR materials.

100 HV respectively. After 50% of cryorolling (50CR), hardness of the eutectic and matrix zones has increased to 105 HV and 95 HV respectively. In 87CR material, the silicon particle distribution is almost uniform in the primary aluminium matrix and the dendritic network is completely eliminated. However, some particle clusters are observed in the ND plane (top face in Fig. 1(d)) and those cluster zones are considered as the eutectic zones for the final processed material. Hardness at those zones is found to be 108 HV and the hardness in the matrix zone is 107 HV. Since the homogeneity in the hardness is not observed in the 50CR material it is not considered for any further studies.

Tensile test is performed to evaluate the mechanical properties. Fig. 8 shows the true stress–strain curves of AC, ST and 87CR materials. The uniform elongation before the onset of local deformation is evaluated based on the considère criterion [19] and is represented by the rectangular box in the figure. The quantified information of mechanical properties such as strength and

Table 3
Dislocation density of ST, 50CR and 87CR materials.

Material	Domain size (Å)	Micro-strain (%)	Dislocation density ($\times 10^{14} \text{ m}^{-2}$)
ST	31813.1	0.052	1.99
50CR	1634.75	0.122	90.24
87CR	898.67	0.101	136.67

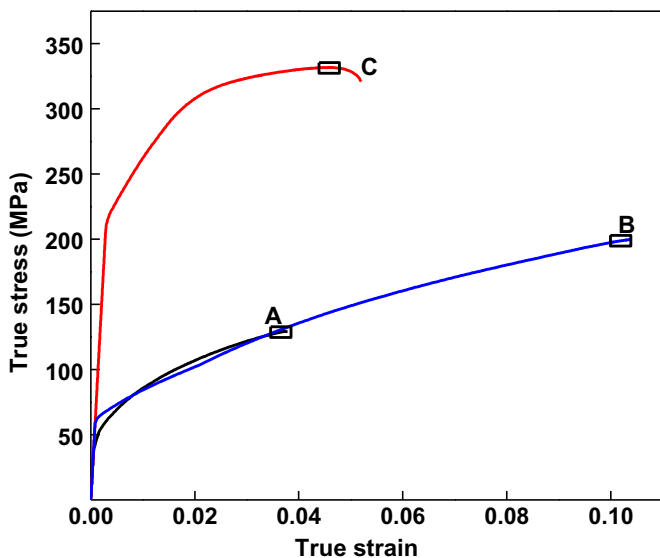


Fig. 8. True stress–strain curve of A – AC; B – ST; C – 87CR material.

Table 4
Mechanical properties of base and processed materials.

	Proof stress (MPa)	Tensile strength (MPa)	Uniform elongation (%)	Total elongation (%)	σ_{UTS}/σ_{YS}
AC	68	129	3.7	3.8	1.9
ST	72	200	10.3	10.4	2.8
87CR	237	332	4.1	5.2	1.4

ductility are represented in **Table 4**.

In the as cast state, the ultimate tensile strength (simply strength, hereafter) and ductility are 129 MPa and 3.8% respectively. After solution treatment, both the strength and ductility increased to 200 MPa and 10.4% respectively. A negligible post-

necking ductility (0.06%) is observed in both AC and ST materials. The tensile strength of cryorolled sample (87CR) has increased to 332 MPa with the uniform elongation of 4.06% and a total ductility of 5.2%.

The mode of failure during the tensile test is analysed by means of OM and SEM fractographs. **Fig. 9** shows the longitudinal section of the fracture surface after tensile testing. The crack path along the dendrite boundaries is observed in case of both AC (**Fig. 9(a)**) and ST (**Fig. 9(b)**) materials. Sub-surface crack initiation is also seen at some matrix–particle interface. After cryorolling, the crack travels in a linear path (**Fig. 9(c)**) and the crack propagation along the matrix zone is shown in **Fig. 9(d)**.

Transverse view of the tensile fracture surface is shown in **Fig. 10**. Large number of dendrite globules are seen both in AC (**Fig. 10(a)** and (**b**)) and ST material (**Fig. 10(c)** and (**d**)) represented by the arrows. The particle–matrix delamination is also evident from the cleavage facets observed in both AC and ST materials (**Fig. 10(b)** and (**d**)).

The fracture surface of the 87CR material is characterized with micro-dimples (**Fig. 10(f)**). Since the dimples are very small, a higher magnification image was taken and is shown in **Fig. 11**. Along with the micro-dimples, some interface shearing is also observed which is characterized by the cleavage facet structure as encircled in **Fig. 11** as zone B.

4. Discussions

4.1. Microstructural evolution

When the AC material was subjected to solution treatment (ST), various microstructural changes take place which are explained with the help of the phase diagram shown in **Fig. 12**. The solid solubility of silicon in aluminium at room temperature is only 0.05 wt% and any composition beyond this forms into a second phase. The high temperature solubility of silicon is about 1.2 wt% at 540 °C [14]. A356 contains about 6.6% of silicon and hence at

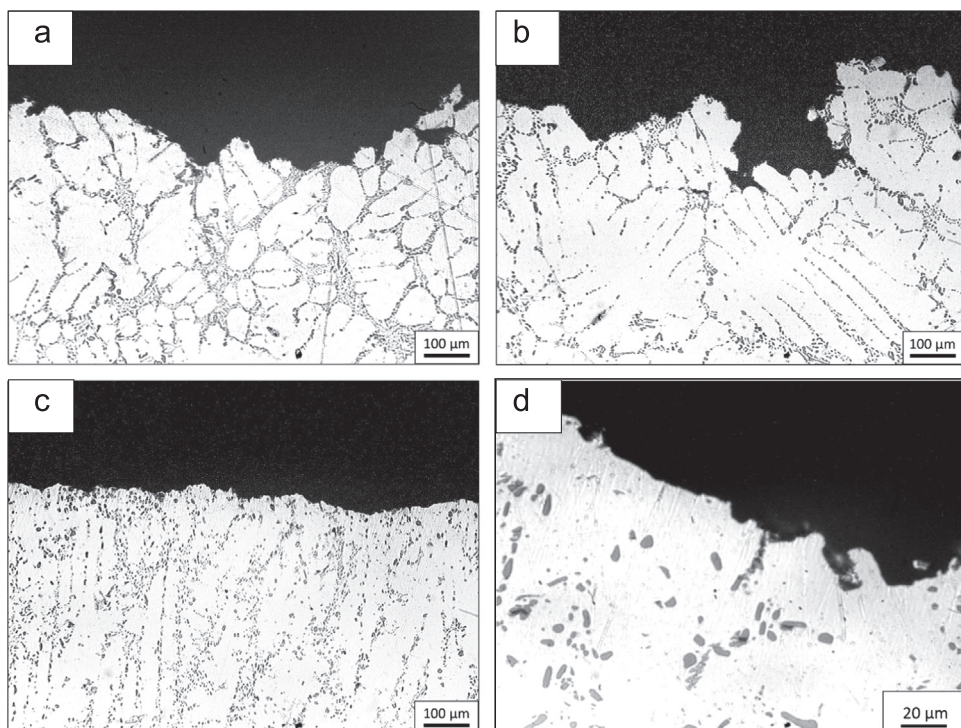


Fig. 9. Longitudinal section of the fracture surface of (a) AC; (b) ST; (c) 87CR materials. (d) shows the magnified view of the crack propagation in 87CR.

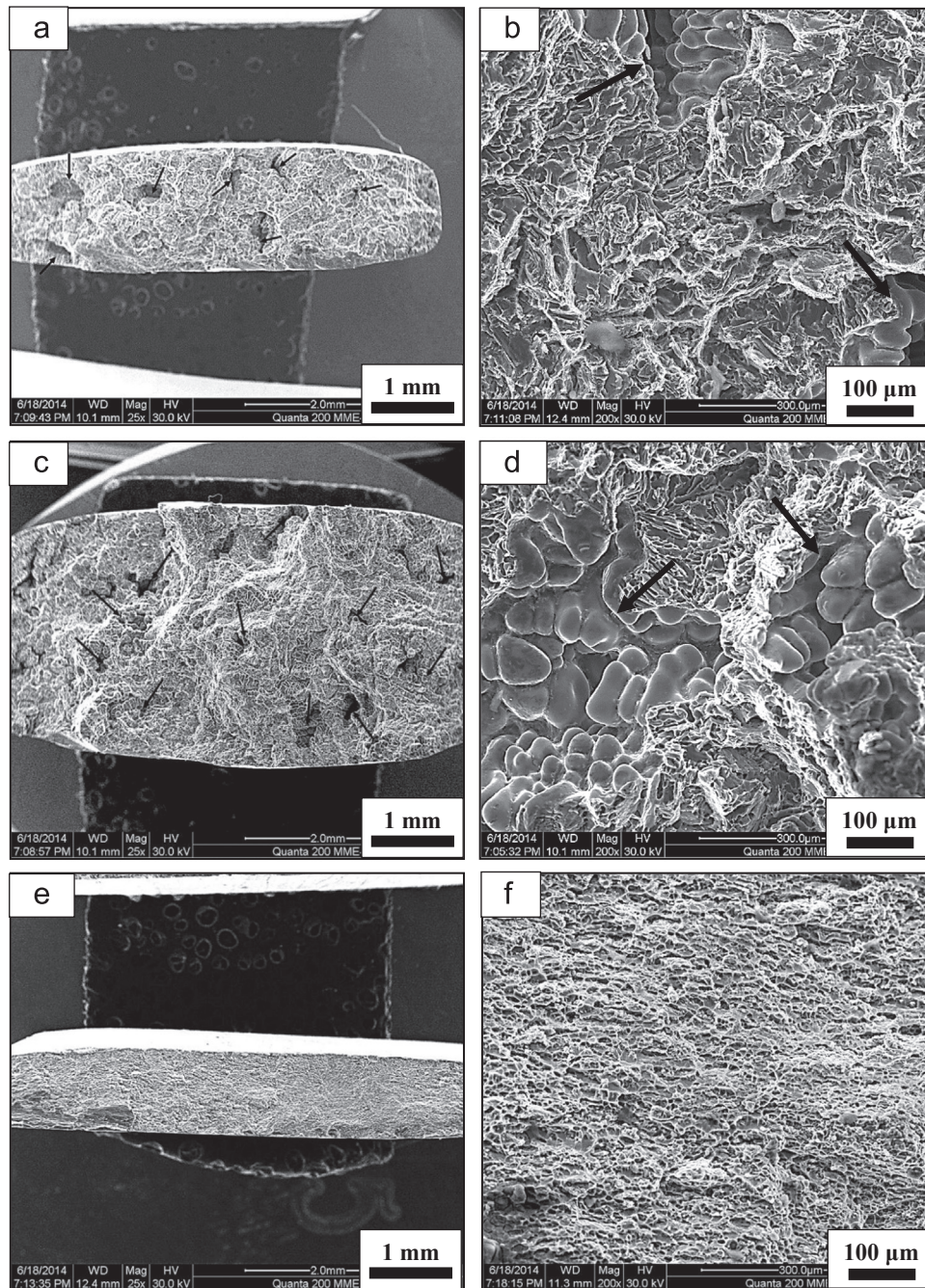


Fig. 10. SEM fractographs showing the fracture surface of (a) & (b) AC; (c) & (d) ST; (e) & (f) 87CR material. The arrows in the images show the porosity.

high temperature part of the aluminium silicon eutectics dissolves into the α -aluminium matrix. Since the sharp edges of these eutectic particles have high surface energy, the atoms in those regions diffuse into the α -aluminium matrix when they are thermally activated. This reduces the aspect ratio of the silicon particles (Fig. 3(e)) and the aspect ratio approaches unity. Other alloying elements such as magnesium and copper also have high positive solubility gradient with temperature and hence dissolve in the aluminium matrix at the solutionizing temperature (540°C). When the sample is rapidly cooled down to room temperature, the solute atoms have no time to diffuse out of the matrix and the matrix becomes a supersaturated solid solution.

As the material is rolled in the liquid nitrogen temperature (cryorolling), there is a series of evolution which takes place in the microstructure. The inherent casting defect, micro-pores are

eliminated during cryorolling. The monotonic plastic flow of the material due to the combined shear and compressive strain imposed during rolling fills the void and makes the material free from micro-voids. The evolution of the silicon particles is explained with the aid of a schematic shown in Fig. 13. During cryorolling, the particles obstruct the dislocation movement and hence accumulation of dislocations takes place at the particle-matrix interface. Because of the high stress concentration at the interface, crack initiates in the particle and then fracturing occurs (Fig. 2(b)).

Because of the spheroidization treatment the initial aspect ratio of the particles is less (Fig. 3(d)) and when these particles shear during cryorolling, the aspect ratio increases with the reduction in the size (Fig. 13). Further, with increase in the cryorolling strain, the sheared particles are subjected to further shear and this is

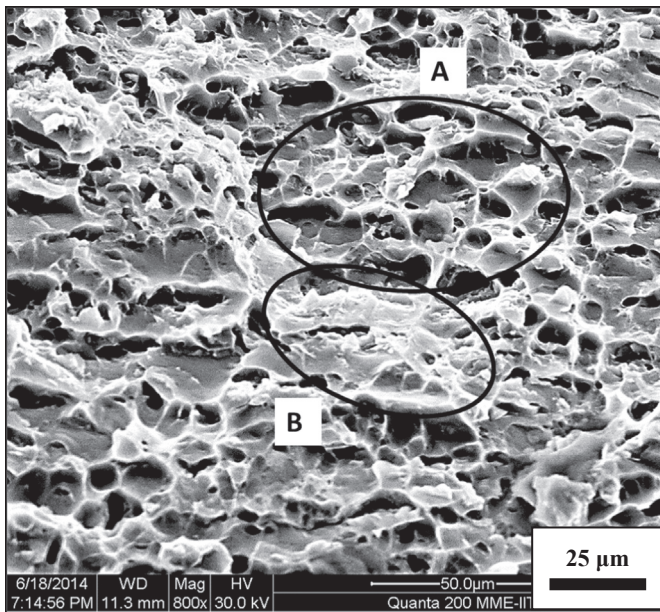


Fig. 11. High magnification fractograph of 87CR material showing micro-dimples (zone A) and interface shear (zone B).

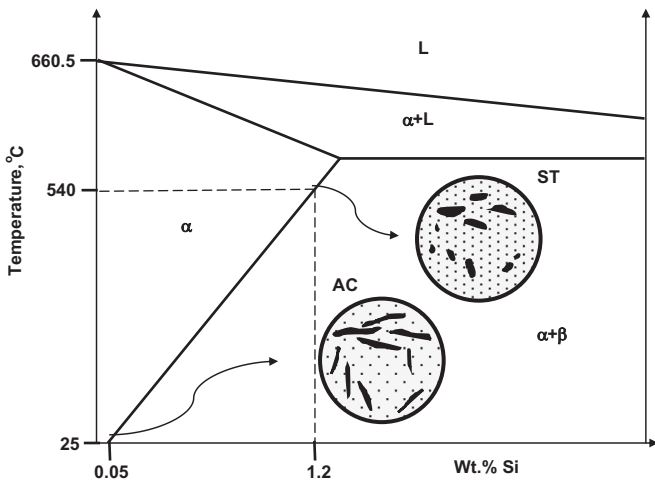


Fig. 12. Phase diagram of the Al-Si alloy system with the insets showing the schematic of the evolution of particles from the cast state during solution treatment.

termed as secondary shear. This secondary shear decreases both the size and aspect ratio of the particles (Fig. 13). The concept of multiple shearing is validated from the observed distribution of the size and aspect ratio of the silicon particles in the ST and CR materials. The particle size is showing a decreasing trend from ST to 87CR materials (Fig. 3), whereas the aspect ratio is increasing upto 50CR material and then decreasing which is evident in 87CR material (Fig. 4).

The refined particles are distributed by the aluminium matrix which is plastically deformed in the rolling process both in the normal and rolling direction due to the compressive and shear strain respectively. Thus the dendritic microstructure as observed in the AC and ST material, gets transformed into an elongated dendritic structure at lower cryorolling strain (50CR) (Fig. 1(c)). With increasing strain, the particles are refined and are more uniformly distributed in the aluminium matrix as observed in 87CR material (Fig. 1(d)).

The plastic deformation during cryorolling induces large amount of dislocation in the aluminium matrix. Since the

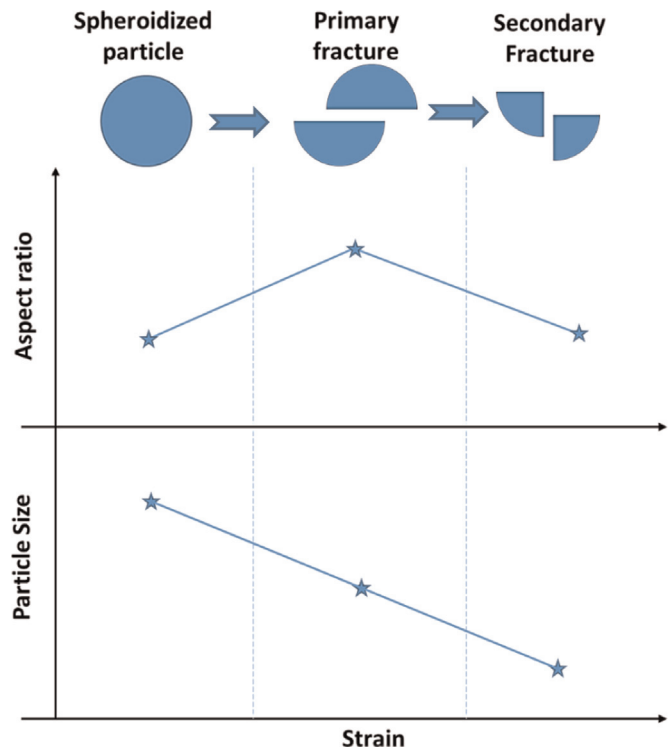


Fig. 13. Schematic layout showing the effect of particle shear on the size and the aspect ratio.

deformation process takes place in cryogenic temperature, dynamic recovery of dislocations is suppressed and hence the dislocation density keeps increasing with cryorolling strain. When the matrix is saturated with the dislocations, they tend to form cell sub-structures by a phenomenon called polygonization [30] (Fig. 5). As the cryorolling strain increases, the sub-grain structures get refined further. The silicon particles hinder the dislocation movement and the dislocations are effectively pinned at the matrix-particle interface. Therefore, the sub-grains at the interface are finer (Fig. 5(d)) when compared with the one in the central matrix zone (Fig. 5(c)). As more substructure evolves, the lattice dislocation decreases with an increase in the cell boundary dislocations. This results in an increase in the boundary density with finer cell-structures. Also, the boundaries that confine the cell-structures are not regular with no preferred orientations [31] and the ratio of atoms covering the boundary zones are more in the fine structured cryorolled material. The boundary zone atoms diffract the incident X-ray in all directions in the X-ray diffraction experiment and this is observed as the increased background intensity in XRD for 87CR material (Fig. 6(b)).

4.2. Mechanical behaviour and strengthening mechanisms

The tensile strength as observed in the present material is in the following order:

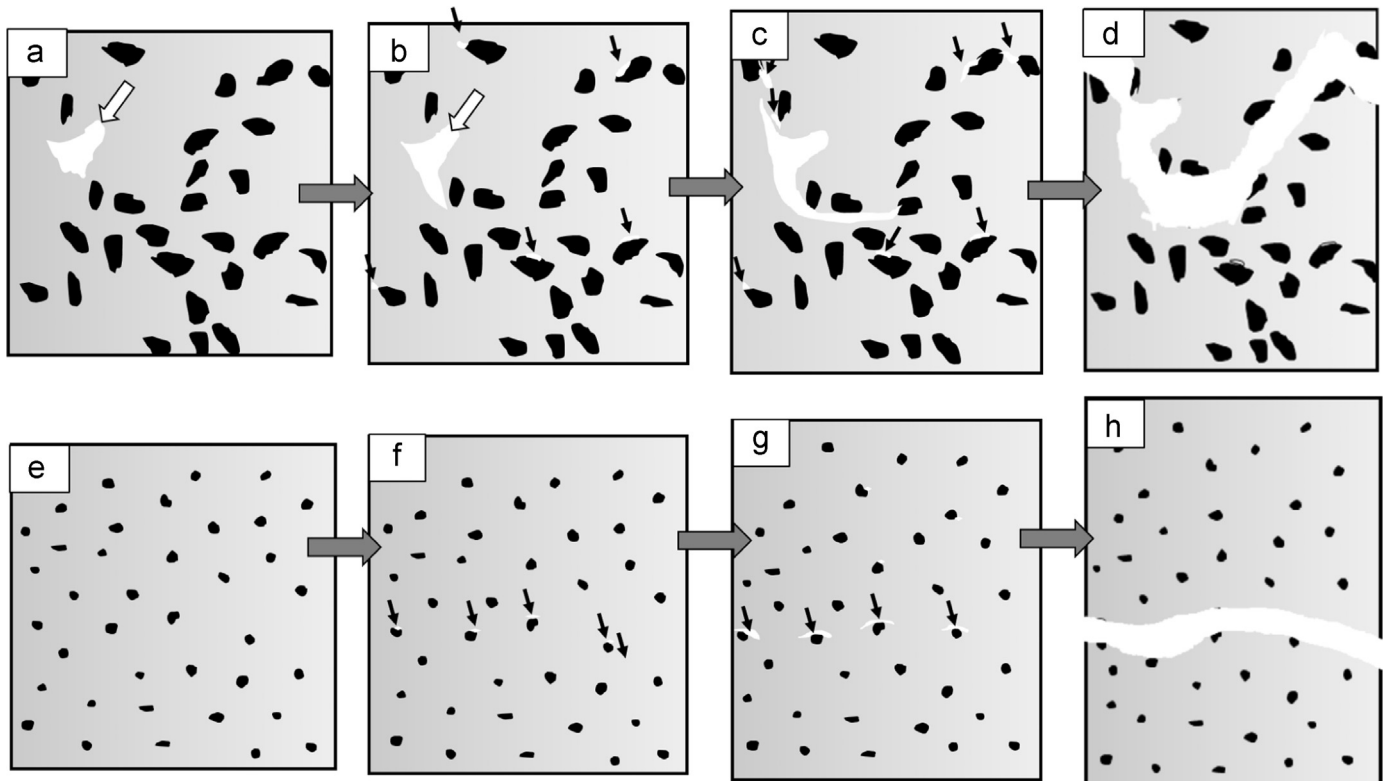
$$\text{AC} < \text{ST} < 50\text{CR} < 87\text{CR}$$

The AC material shows the least strength of 129 MPa. In AC material, the sharp silicon particles (Fig. 1(a)) act as stress risers and give rise to premature material failure which is the reason for its less strength and ductility. After solution treatment, the strength of the material increases to 200 MPa. The reason for the strength increment in ST material is due to the solid-solution strengthening. In A356, the alloying elements like silicon, magnesium and copper are dissolved in the aluminium matrix during solution treatment because of its higher solubility at elevated temperature and are retained in the aluminium lattice upon rapid

Table 5

Various SPD techniques employed on Al-Si cast alloy system and their effect on the mechanical properties.

Reference	Material (Al-x% Si)	Process	Strain imposed	Mechanical properties		Enhancement (%)	
				UTS (MPa)	ϵ_f (%)	UTS	ϵ_f
[32]	Al-12.2% Si	ECAE: A ^a @ 473K	6.9	180	10.1	47	359
[33]	Al-11% Si	RD-ECAP ^b @ 573K	36.8	250 ^e	14 ^e	14	600
[34]	Al-7% Si	HPT ^c : 6 GPa @ 298 K	92.5	240 ^e	85 ^e	79	112
[35]	Al-7% Si	ECAP: A @ RT	9.2	248 ^e	22 ^e	60	47
[36]	Al-2% Si	FSP ^d	—	160 ^e	42	3	180
Present work	Al-7% Si	ECAP: B _C @ RT	4	271	—	170	—
		CR	2.08	332	5	157	39

^a Equal channel angular extrusion;^b Rotary die – equal channel angular pressing;^c High pressure torsion;^d Friction stir processing;^e Data are extracted from the stress-strain plots.**Fig. 14.** Schematic diagram showing the mode of failure. (a)–(d) shows the failure mechanism in AC & ST material. Zone marked by white arrows are micro-pores. (e)–(h) shows the failure mechanism in 87CR material. In both the case tensile loading is considered to be applied in the vertical direction.

cooling. The contribution of various solutes to the strength of the matrix is calculated based on the equation [28]

$$\Delta\sigma_{ss} = MGbe_{ss}^{\frac{3}{2}}\sqrt{c} \quad (3)$$

where M is the orientation factor which is 3.06 for FCC material, G is the shear modulus, b is the Burgers vector, c is the solute concentration and ϵ is the lattice strain. From the equation, it is observed that the strengthening effect is greatly influenced by the lattice strain and then by the concentration of the solute atom in the matrix. Since the difference in radii between silicon (1.17 Å) and aluminium (1.25 Å) is not much, the contribution of silicon atom towards solid solution strengthening is less with 9.2 MPa wt%⁻¹. Magnesium (1.45 Å) gives the maximum strengthening coefficient of 18.6 MPa wt%⁻¹ [28] and copper with a strengthening coefficient of 13.8 MPa wt%⁻¹. Based on the above analysis, the overall solid solution strengthening contribution is

calculated as 19 MPa. As compared to the AC material, the observed strength increment in ST material is about 70 MPa. However, the calculated strength increment is very less (19 MPa) than the obtained result. The possible reason may be spheroidization of sharp silicon particles which reduces the chance of premature failure, increasing both the strength and ductility in ST material.

After cryorolling (87CR), the strength of the material is increased to 332 MPa. Since the rolling is performed at liquid nitrogen temperature, the solutes are not thermally activated to diffuse out of the aluminium matrix. Therefore, the aforementioned solid-solution strengthening is also valid for 87CR material. Apart from this, the CR materials have large amount of stored dislocations which contributes to its increase in strength. The strength increment because of the dislocations, $\Delta\sigma_d$ is calculated using the relation [28]:

$$\Delta\sigma_d = M\alpha Gb\Delta\rho^{\frac{1}{2}} \quad (4)$$

where α is a dimensionless constant equal to 0.2 and $\Delta\rho$ is the increase in the dislocation density. The dislocation density increases from $2 \times 10^{14} \text{ m}^{-2}$ in ST to $1.4 \times 10^{16} \text{ m}^{-2}$ in 87CR material. The increase in the dislocation density ($\Delta\rho$) is found to be $138 \times 10^{14} \text{ m}^{-2}$ for 87CR. The calculated increment in the strength because of the accumulated dislocations is found to be 528 MPa for 87CR material. Though the calculated increase in the strength by dislocation strengthening is 528 MPa, the complete strength contribution from the dislocation is not realised in 87CR (332 MPa). This is because of the high dislocation pileup at the particle–matrix interface. The dislocation density is more at the interface zone than that at the central matrix zone (Fig. 5(d) and (c)). Therefore, the interface zone gets saturated with dislocations before the matrix zone during tensile test and crack initiates at the interface. The same is validated by the micro-indentation hardness test at the eutectic zone (Fig. 7). It is observed that the hardness of the eutectic zone increase from 100 HV in ST material to 105 HV in 50CR material. Then, the hardness at the eutectic zone gets saturated and hence no significant increase is observed in 87CR material though the hardness of the matrix zone increased from 82 HV in 50CR to 107 HV in 87CR.

The enhancement in the mechanical properties by cryorolling is compared with the mechanical properties of similar Al–Si cast alloy systems subjected to various other severe plastic deformation techniques and given in Table 5. It is observed that the present cryorolling process gave the maximum increase in strength of about 157%. In all the other SPD techniques, the working temperature is high and hence dynamic recrystallization takes place during SPD processing, leading to fine/ultrafine grained microstructure. Therefore, the strengthening mechanism in all the other processed material is dominated by grain boundary strengthening. Ma et al. [28] calculated the strengthening contribution due to grain boundary in Al 7075 based on Hall–Petch relationship and found a maximum of 242 MPa for the average grain size of 245 nm which is a nominal size achieved by many SPD techniques. Also, it is a known fact that aluminium possesses high stacking fault energy (SFE) and hence it is more prone to dynamic recovery. The SFE of Al–Si–Mg alloy system is found to be 150 mJ m^{-2} [17] even after various alloying elements. Therefore, when these materials are subjected to any of the high temperature deformation, dislocation annihilation takes place due to dynamic recovery. Hence, large strains were needed in other SPD techniques to refine the grains. Cryogenic processing prevents annihilation of dislocation resulting in accumulation of more dislocations in the matrix with an imposed strain of 2.08. Because of the high dislocation density in the cryorolled material, the dominating strengthening mechanism is dislocation strengthening. It is found that the strengthening factor by dislocation is about twice than that of the grain boundaries. Therefore cryorolled material shows an extraordinary strength of 332 MPa which is almost 100 MPa more than the highest achieved by any other SPD processed material in the similar Al–Si alloy series.

4.3. Failure mechanisms

The mode of failure of the AC, ST and 87CR materials are analysed with a schematic shown in Fig. 14. Both the AC and ST material has dendritic microstructure with coarse silicon particles and hence the fracture mechanism is same for both the materials. The AC and ST materials have inherent casting porosity and this porosity is a stress riser which leads to crack initiation at its vicinity (Fig. 14(a)). Apart from the micro-pores, the matrix–particle interface is identified as another weak zone. The sharp edges are

the potential sites for crack initiation (Fig. 14(b)). The propagation of crack in AC and ST material is inter-dendritic i.e. the crack travels along the dendrite boundary (Fig. 14(c)). Fig. 9(a) and (b) shows the crack path in AC and ST materials respectively which shows that in both the materials, the crack propagation is inter-dendritic. The micro-cracks enlarge and the material, finally fails by coalescence of cracks (Fig. 14(d)).

In cryorolled material, the dendritic network is completely eliminated and the particles are fragmented and finely distributed in the matrix. Therefore, the model of inter-dendritic failure as observed in AC and ST materials is no more valid. In 87CR material, the crack initiates at the weak matrix–particle interface (Fig. 14(f)) and then propagates through the matrix (Figs. 14(g) and 9(d)). Since the matrix is ductile, the fracture surface in this zone is characterized by micro-dimples. Fig. 11 shows the surface fractography of the 87CR material in which large number of micro-dimples are seen which are marked as zone A. Also, the particle–matrix interface zones are characterized by facet structures (Zone B) which shows the crack initiation at the interface. However, the overall ductility of the cryorolled material is less. This is because of the presence of high dislocation density in the matrix zone which acts as barrier for movement of mobile dislocations during tensile straining, leading to a decrease in the ductility.

5. Conclusions

The major conclusions from the current research work is summarized below:

1. Cryorolling was successfully performed in a hypoeutectic cast Al–Si alloy (A356) upto a thickness reduction of 87.5%.
2. Cryorolling resulted in complete elimination of casting porosity, transformation of dendrite structure to dislocation subcells, refinement and uniform distribution of coarse silicon particles.
3. The strength of the cryorolled material is found to be 150% higher than that of as cast material without much loss in the ductility. The improvement in the mechanical properties is attributed to the fine distribution of second phase particles and formation of fine structures with high dislocation density in the aluminium matrix.
4. The improvement in the mechanical properties by cryorolling is compared with the existing literature on SPD of similar cast Al–Si alloys and it is found that the present work leads to a significant increase in the strength than any of the other SPD techniques at a very low imposed strain of about 2.
5. Fractography studies revealed that the dendrite network in the as cast and solution treated material cause inter-dendritic fracture and the fracture mechanism is changed after cryorolling and the crack propagation is found to be trans-dendritic in cryorolled material.

References

- [1] G. Purcek, O. Saray, O. Kul, Met. Mater. Int. 16 (2010) 145.
- [2] A. Tewari, S. Mishra, S. Tiwari, Trans. Indian Inst. Met. 62 (2009) 343.
- [3] T.S. Mahmoud, Surf. Coat. Technol. 228 (2013) 209.
- [4] R. Jamaati, S. Amirkhanlou, M.R. Toroghinejad, B. Niroumand, Mater. Sci. Eng. A 528 (2011) 2495.
- [5] M. Moradi, M. Nili-Ahmababadi, B. Heidarian, Int. J. Mater. Form. 2 (2009) 85.
- [6] P.R. Guru, F. Khan MD, S.K. Panigrahi, G.D.J. Ram, J. Manuf. Process. 18 (2015) 67.
- [7] A. Knutinen, K. Nogita, S.D. McDonald, A.K. Dahle, J. Light Met. 1 (2001) 229.
- [8] A.M.A. Mohamed, A.M. Samuel, F.H. Samuel, H.W. Doty, Mater. Des. 30 (2009) 3943.

- [9] M. Zhu, Z. Jian, G. Yang, Y. Zhou, *Mater. Des.* 36 (2012) 243.
- [10] R.Z. Valiev, R.K. Islamgaliev, I.V. Alexandrov, Bulk Nanostructured Materials from Severe Plastic Deformation, 2000.
- [11] Y. Estrin, A. Vinogradov, *Acta Mater.* 61 (2013) 782.
- [12] I. Sabirov, M.Y. Murashkin, R.Z. Valiev, *Mater. Sci. Eng. A* 560 (2013) 1.
- [13] I. Gutierrez-Urrutia, M.a. Muñoz-Morris, D.G. Morris, *Acta Mater.* 55 (2007) 1319.
- [14] C.M. Cepeda-Jiménez, J.M. García-Infanta, A.P. Zhilyaev, O.A. Ruano, F. Carreño, *J. Alloy. Compd.* 509 (2011) 636.
- [15] Z.Y. Ma, R.S. Mishra, M.W. Mahoney, *Scr. Mater.* 50 (2004) 931.
- [16] M. Shaban Ghazania, A. Vajdb, B. Mosadeg, *J. Adv. Mater. Process.* 2 (2014) 47.
- [17] V.S. Sarma, J. Wang, W.W. Jian, A. Kauffmann, H. Conrad, J. Freudenberger, Y. T. Zhu, *Mater. Sci. Eng. A* 527 (2010) 7624.
- [18] D. Ke, L. Hengcheng, J. Qiumin, T. Yun, *Mater. Sci. Eng. A* 527 (2010) 6887.
- [19] Y. Wang, M. Chen, F. Zhou, E. Ma, *Lett. Nat.* 419 (2002) 912.
- [20] S. Cheng, Y.H. Zhao, Y.T. Zhu, E. Ma, *Acta Mater.* 55 (2007) 5822.
- [21] S.K. Panigrahi, R. Jayagathan, *Metall. Mater. Trans. A* 41 (2010) 2675.
- [22] N.N. Krishna, K. Sivaprasad, P. Susila, *Trans. Nonferrous Met. Soc. China* 24 (2014) 641.
- [23] M.V. Markushev, E.V. Avtokratova, I.Ya Kazakulov, S.V. Krymsky, M. Yu. Mochalova, M.Yu. Murashkin, O.Sh. Sirdikov, *Russ. Metall.* 4 (2011) 364.
- [24] N. Naga Krishna, K. Sivaprasad, P. Susila, *Trans. Nonferrous Met. Soc. China* 24 (2014) 641.
- [25] B. Gopi, N. Naga Krishna, K. Sivaprasad, K. Venkateswarlu, *Adv. Mater. Res.* 584 (2012) 556.
- [26] W.S. Rasband, *ImageJ*, 2014.
- [27] G. Williamson, W. Hall, *Acta Metall.* 1 (1953) 22.
- [28] K. Ma, H. Wen, T. Hu, T.D. Topping, D. Isheim, D.N. Seidman, E.J. Lavernia, J. M. Schoenung, *Acta Mater.* 62 (2014) 141.
- [29] H. Wen, T.D. Topping, D. Isheim, D.N. Seidman, E.J. Lavernia, *Acta Mater.* 61 (2013) 2769.
- [30] M. Moradi, M. Nili-Ahmabadi, B. Poorganji, B. Heidarian, M.H. Parsa, T. Furuhara, *Mater. Sci. Eng. A* 527 (2010) 4113.
- [31] P. Keblinski, D. Wolf, S. Phillpot, H. Gleiter, *Scr. Mater.* 41 (1999) 631.
- [32] T. Kucukomeroglu, *Mater. Des.* 31 (2010) 782.
- [33] A. Ma, M. Takagi, N. Saito, H. Iwata, Y. Nishida, K. Suzuki, I. Shigematsu, *Mater. Sci. Eng. A* 408 (2005) 147.
- [34] T. Mungole, P. Kumar, M. Kawasaki, T.G. Langdon, *J. Mater. Res.* 29 (2014) 2534.
- [35] J.M. Garcia-Infanta, A.P. Zhilyaev, F. Carreño, O.A. Ruano, J.Q. Su, S.K. Menon, T. R. McNelley, *J. Mater. Sci.* 45 (2010) 4613.
- [36] K. Venkateswarlu, G. Das, A.K. Pramanik, C. Xu, T.G. Langdon, *Mater. Sci. Eng. A* 427 (2006) 188.